SCIENCE CHINA
Information Sciences

• LETTER •

November 2025, Vol. 68, Iss. 11, 219402:1–219402:2
https://doi.org/10.1007/s11432-024-4476-5

A hybrid-integrated GaN Doherty PA module with output harmonic control for small cells

Xiyu WANG[1], Xiaolin LV[2*], Wenming LI[2], Dehan WANG[1,2], Kai CUI[2] & Wenhua CHEN[3]

[1]*State Key Laboratory of Mobile Network and Mobile Multimedia Technology, Shenzhen 518055, China*
[2]*RCH System Design Department of ZTE Corporation, Xi'an 710100, China*
[3]*Institute of Microwave & Antenna, Tsinghua University, Beijing 100084, China*

Received 28 October 2024/Revised 1 April 2025/Accepted 5 June 2025/Published online 19 September 2025

Citation Wang X Y, Lv X L, Li W M, et al. A hybrid-integrated GaN Doherty PA module with output harmonic control for small cells. Sci China Inf Sci, 2025, 68(11): 219402, https://doi.org/10.1007/s11432-024-4476-5

In 5G small cell applications, integrating Doherty power amplifier (DPA) is essential to minimize the occupied area and enable higher channel density. Existing integrated DPA modules generally lack effective output harmonic control [1–4], which leads to suboptimal PA efficiency. This deficiency limits the overall efficiency of the system and makes the PA performance more susceptible to input nonlinearity and variations in output harmonic impedance [5].

This study proposes a network that combines the DPA with output harmonic control. The carrier of the combining network has the second harmonic open-circuit characteristic of the inverse class-F (F^{-1}) PA while maintaining the advantage of a compact structure. We designed a hybrid-integrated DPA module operating in the 2.5–2.7 GHz frequency, which benefits from the proposed combining network and corresponding design method, yielding excellent simulation and measured results.

Combining network with harmonic control. Figure 1(e) shows the proposed combining network. Considering the significance of carrier efficiency in DPA performance, the second harmonic control characteristic is preferentially introduced to the carrier.

Firstly, it is necessary that the combining network and the quarter-wavelength ($1/4\lambda$) line following the carrier shown in Figure 1(a) maintain a consistent ABCD parameter matrix,

$$\begin{bmatrix} 0 & \mathrm{j}Z_0 \\ \mathrm{j}Y_0 & 1 \end{bmatrix}. \tag{1}$$

Next, to absorb the C_{ds} of the HEMT into the combining network, a CLC π-type structure is selected for transformation, as shown in the gray part of Figure 1(b), and it satisfies (2) below. Here, C_1 can be a negative capacitance,

$$C_\pi = C_{ds} + C_1 = \frac{1}{Z_0\omega_0},\ L_\pi = \frac{Z_0}{\omega_0}. \tag{2}$$

Subsequently, π-T transformation is conducted, as shown in Figure 1(c) and (3). After the transformation, the inconvenience of implementing the positive C_1 at the drain of the discrete HEMT is avoided. It is of note that C_2 does not necessarily have to be positive,

$$\begin{aligned} &L_{T1} = \frac{L_\pi}{1 + C_1\left(\frac{C_\pi - C_2}{C_2 C_\pi}\right)},\ L_{T2} = \frac{L_\pi}{1 + C_2\left(\frac{C_\pi - C_1}{C_1 C_\pi}\right)}, \\ &C_{T1} = C_1 + C_2 - \frac{C_1 C_2}{C_\pi},\ C_{T2} = C_\pi - C_2. \end{aligned} \tag{3}$$

Finally, to complete the impedance inverted and thereby achieve the second harmonic open-circuit characteristic on the current source plane required by the F^{-1}, a short-circuit point is introduced at the position where the second harmonic transmission phase shift in the network is 90°. Then, it is necessary to satisfy (4) for C_{ds}, L_{T1} and Y_3,

$$C_{ds}L_{T1} = \frac{1}{4\omega_0^2},\ Y_3 = \mathrm{j}wC'_{T1} = \begin{cases} \mathrm{j}wC_{T1}, & w = w_0, \\ \infty, & w = 2w_0. \end{cases} \tag{4}$$

The requirement for Y_3 in (4) can be achieved by means of the structure in the purple area of Figure 1(d) under the premise of (5). As Eq. (4) specifies C_2, the network parameters except C_{T1} in the previous step become a unique solution again, and the newly added L_{p1} in this step becomes a new independent parameter for controlling the equivalence of C'_{T1} to C_{T1} at frequencies other than w_0.

$$L_{p2} = \frac{L_{p1}}{3\left(1 + w_0^2 L_{p1} C_{T1}\right)},\ C_{p2} = \frac{3\left(1 + w_0^2 L_{p1} C_{T1}\right)}{4w_0^2 L_{p1}}. \tag{5}$$

By simultaneously solving (2)–(5), the complete analytical solution of the proposed combining network can be obtained. It is of note that second-order resonance is introduced from Figures 1(a)–(d), and owing to the inherent narrowband nature of resonance, the small signal matching bandwidth typically experiences degradation. Fortunately, this degradation does not have a significant impact on the

* Corresponding author (email: lv.xiaolin@zte.com.cn)

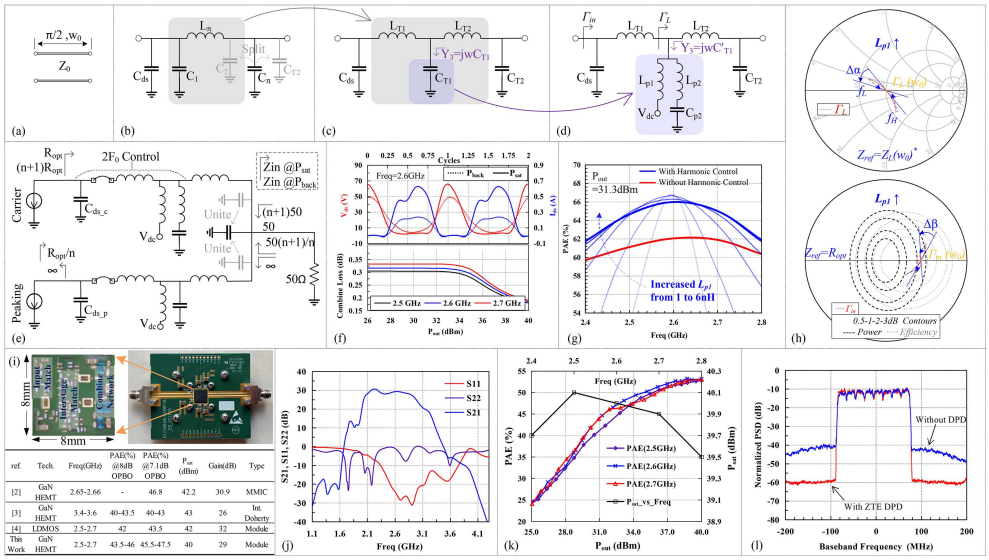

ref.	Tech.	Freq(GHz)	PAE(%) @6dB OPBO	PAE(%) @7.1dB OPBO	P_{sat} (dBm)	Gain(dB)	Type
[2]	GaN HEMT	2.65-2.66	-	46.8	42.2	30.9	MMIC
[3]	GaN HEMT	3.4-3.6	40-43.5	40-43	43	26	Int. Doherty
[4]	LDMOS	2.5-2.7	42	43.5	42	32	Module
This Work	GaN HEMT	2.5-2.7	43.5-46	45.5-47.5	40	29	Module

Figure 1 (Color online) (a) 1/4λ line; (b) lumped CLC π-type equivalent; (c) π-T transformation; (d) second-order resonance equivalent; (e) proposed combining network; (f) simulation results: combining loss and the waveforms of V_{ds} and I_{ds}; (g) PAE of both the proposed network and traditional network; (h) bandwidth compensation mechanism of $P_{\rm out}$ and DE; (i) photos of the module and EVB and performance comparison table; (j) measurement results of S-parameters; (k) measurement results of PAE and $P_{\rm sat}$; (l) spectrum output from the proposed module before and after pre-distortion.

performance of the PA because the design of the PA focuses more on power match rather than conjugate match. The degree of freedom L_{p1} here generates a beneficial compensation mechanism for the efficiency bandwidth in the PA back-off region, which is introduced as follows:

$$C'_{T1} = \frac{(\frac{w}{w_0})^2 - 1}{w^2 L_{p1}[1 - (\frac{w}{2w_0})^2]} + \frac{3C_{T1}}{4[1 - (\frac{w}{2w_0})^2]}. \quad (6)$$

The C'_{T1} exhibits a positive correlation with L_{p1} when $w < w_0$ and a negative correlation when $w_0 < w < 2w_0$. This causes L_{p1} to have a regulatory effect on the trajectory of Γ_L, as shown in Figure 1(h). When L_{p1} increases, the trajectory of Γ_L rotates counterclockwise around $\Gamma_{L(w_0)}$ and contracts.

$$\Gamma_{\rm in} = f(\Gamma_L) = \frac{S_{11} + (S_{12}S_{21} - S_{11}S_{22})\Gamma_L}{1 - S_{22}\Gamma_L}, S_{12}S_{21} \neq 0. \quad (7)$$

Eq. (7) shows that f belongs to a fractional linear map. Then, at w_0, the map from Γ_L to $\Gamma_{\rm in}$ has conformality ($\Delta\beta = \Delta\alpha$) and invariance of the expansion rate. This also means that L_{p1} indirectly regulates the rotation and expansion of $\Gamma_{\rm in}$. Thus, when the trajectory of $\Gamma_{\rm in}$ rotates around $\Gamma_{{\rm in}(w_0)}$ to be close to the long axis direction of the olive-shaped power contours, the number of power and efficiency contours intersecting with $\Gamma_{\rm in}$ effectively decreases. As a result, the bandwidth of efficiency can be effectively compensated without having to pursue the maximization of the small signal matching bandwidth. Taking Figures 1(b) and (d) as the output match of the class-AB PA, the simulation results confirm that the back-off efficiency bandwidth of the proposed network is similar to that of the traditional network under appropriate values of the L_{p1}, as illustrated in Figure 1(g).

Application in DPA module. The designed module is composed of a class-AB PA driving a DPA, and all the PAs are fabricated using 0.25 μm GaN on SiC technology. The DPA utilizes HEMTs with total gate widths of 1.1 and 1.8 mm. The combining network is implemented with 0201 and 0402 series high-Q SMDs attached to the top layer of the multilayer substrate, and the devices of both technologies are assembled together in an LGA 8 mm × 8 mm package, as shown in Figure 1(i). Solid metal vias are used to enhance the heat dissipation capability, and bonding wires are used for interconnection. According to Figure 1(f), the DPA operates in an approximately F^{-1} state. Measurements indicate that within the frequency range of 2.5–2.7 GHz, the $P_{\rm sat}$ remains at 39.9 dBm; the PAE is 42%–45% at an $P_{\rm avg}$ of 31.3 dBm, as shown in Figure 1(k); the drain efficiency exceeds 43.4%; the ACPR is less than −48.5 dBc at an $P_{\rm avg}$ of 31.3 dBm with a 160 MHz LTE signal has a PAR of 8.5 dB, as shown in Figure 1(l). According to the table in Figure 1(i), this study demonstrates competitive efficiency compared to state-of-the-art techniques.

Acknowledgements The authors would like to extend their gratitude to colleagues from ZTE for the assistance provided during the chip testing.

References

1 Gustafsson D, Cahuana J C, Kuylenstierna D, et al. A wideband and compact GaN MMIC Doherty amplifier for microwave link applications. IEEE Trans Microwave Theor Techn, 2013, 61: 922–930
2 Kim C H, Park B. Fully-integrated two-stage GaN MMIC Doherty power amplifier for LTE small cells. IEEE Microw Wireless Compon Lett, 2016, 26: 918–920
3 Maroldt S, Ercoli M. 3.5-GHz ultra-compact GaN class-E integrated Doherty MMIC PA for 5G massive-MIMO base station applications. In: Proceedings of the 12th European Microwave Integrated Circuits Conference, Nuremberg, 2017. 196–199
4 Ladhani H, Maalouf E, Jones J, et al. A compact, 42% PAE, two-stage, LDMOS Doherty PA module for massive MIMO applications. In: Proceedings of IEEE MTT-S International Microwave Conference on Hardware and Systems for 5G and Beyond (IMC-5G), Atlanta, 2019. 1–3
5 Dhar K S, Sharma T, Darraji R, et al. Impact of input nonlinearity on efficiency, power, and linearity performance of GaN RF power amplifiers. In: Proceedings of IEEE International Microwave Symposium (IMS), Los Angeles, 2020. 281–284